

# Phase and amplitude modulation with acoustic holograms

Cite as: Appl. Phys. Lett. **115**, 053701 (2019); doi: [10.1063/1.5110673](https://doi.org/10.1063/1.5110673)

Submitted: 20 May 2019 · Accepted: 9 July 2019 ·

Published Online: 29 July 2019



View Online



Export Citation



CrossMark

Michael D. Brown<sup>a)</sup>

## AFFILIATIONS

Department of Medical Physics and Biomedical Engineering, University College London, Gower St., London WC1E 6BT, United Kingdom

<sup>a)</sup>Electronic mail: [Michael.brown.13@ucl.ac.uk](mailto:Michael.brown.13@ucl.ac.uk)

## ABSTRACT

Acoustic holograms are a low cost method for generating arbitrary diffraction limited pressure distributions in 3 dimensions. However, at present, the creation of complex fields using this approach is limited by the inability of these holograms to independently modulate both the phase and amplitude of an incident wave. In this work, it is shown that this limitation can be circumvented by using two phase holograms, designed using an iterative Fourier transform algorithm, to form the phase conjugate of a back-propagated target pattern over a predefined surface. An experimental test-case, designed to generate the letters “UCL” with the uniform amplitude and phase, is prepared to demonstrate the feasibility of this technique. Field measurements from this sample show that the modulation of both the phase and amplitude of the acoustic field can be achieved with this approach.

© 2019 Author(s). All article content, except where otherwise noted, is licensed under a Creative Commons Attribution (CC BY) license (<http://creativecommons.org/licenses/by/4.0/>). <https://doi.org/10.1063/1.5110673>

The ability to arbitrarily shape acoustic wavefronts is vital for a diverse range of applications in physical acoustics.<sup>1–5</sup> Traditionally, this has been achieved using piezoelectric arrays; however, recently, there has been increasing interest in different acoustic metamaterials and lenses as a potentially cheaper alternative.<sup>6–8</sup> One such an approach, first demonstrated in the 1990s,<sup>9</sup> is to use an acoustic hologram or a phase conjugate lens in conjunction with a single element transducer. With this method, a lens (often 3-D printed) is used to apply a predefined phase map to the output of a transducer at a particular frequency using variations in thickness and sound speed. This phase map is designed to diffract the field to form the desired acoustic pattern.

Acoustic holograms are cheap to manufacture, scale easily to larger apertures, and can operate at high frequencies compared to most metamaterials. However, at present, a limitation is that these holograms are unable to independently modulate both the phase and amplitude of an incident wave. For generating an arbitrary “amplitude” distribution  $A(x, y, z)$ , this is not a significant problem. A range of algorithms have been described which can be used to calculate phase holograms that generate fields with the desired amplitude distribution.<sup>10</sup> However, these typically allow the phase over the target pattern to vary freely. Efficiently coupling energy into and accurately forming an arbitrary complex field  $A(x, y, z)e^{i\phi(x,y,z)}$ , where the phase

is also constrained, is a greater challenge. A range of algorithms have also been described which aim to address this problem.<sup>8,11,12</sup> For example, phase only maps can be found which control both the phase and amplitude within a limited spatial region using conjugate gradient descent or direct binary search.<sup>11,13</sup> However, this is at the expense of decreased energy utilization efficiency and results in significant clutter outside the controlled region for many target fields.

If a holographic lens could modulate both the amplitude and phase, this challenge would be simple to overcome. It would just be necessary to back-propagate the target field to the hologram surface and then create the conjugate field over this surface.<sup>14</sup> In principle, the creation of such a phase and amplitude modulating hologram could be achieved by exploiting different fabrication methods, for example, two material 3-D printing using materials with different sound speeds and absorption. However, if the conjugate field has large variations in amplitude, then a significant fraction of the energy will be lost via absorption. A more efficient approach has been previously reported in optics.<sup>15</sup> This employs two, spatially separate, phase holograms. The first hologram is used to control the amplitude of the field incident on the second hologram. The second hologram then adjusts the incorrect but known phase distribution such that an arbitrary complex field is formed.<sup>16</sup> The goal of this work was to demonstrate that an analogous method can be applied in acoustics.

Several geometries for the two holograms are possible, and three are illustrated in Fig. 1 in the [supplementary material](#). An in-line geometry attaching the first hologram directly to the planar transducer and modulating the amplitude over a parallel plane containing the second hologram which adjusts the phase on transmission is simple to register and implement (Fig. 1(a) in the [supplementary material](#) and Fig. 1). However, this has two drawbacks. First, standing waves could form between the two holograms. Second, the hologram requires some minimum thickness or buffer for structural stability. Waves coupling into this buffer on the second hologram will undergo refraction. This refraction needs to be modeled in the design phase introducing additional complexity. The second drawback can be eliminated by flipping the first hologram and filling the area between the two with a buffer of the same material [Fig. 1(b) in the [supplementary material](#)]. However, the attenuation of most suitable polymers is relatively high (>3 db cm MHz), so absorption is an issue. Another alternative is to use the second hologram as a reflecting element [Fig. 1(c) in the [supplementary material](#)]. Here, as before, the first hologram is directly attached to the transducer. The second hologram, however, operates as a reflecting element rotated by 45° relative to the first. This eliminates standing waves and significantly reduces absorption. However, registering the two is a greater challenge, and higher manufacturing accuracy is required to fabricate the reflecting element as the thickness variations needed to introduce a given phase change are smaller. For this work, the first geometry was chosen. The energy transmission from the hologram material into water at normal incidence is high (0.89), so the effect of standing waves will be minor. To account for refraction, a full-wave model-based approach was adopted for the design.

The aim of the design process was to calculate two phase holograms positioned on two separate planes (see Fig. 1) that combine to generate a complex target pattern at a set depth from an input source (in this work a planar single element transducer). This target pattern

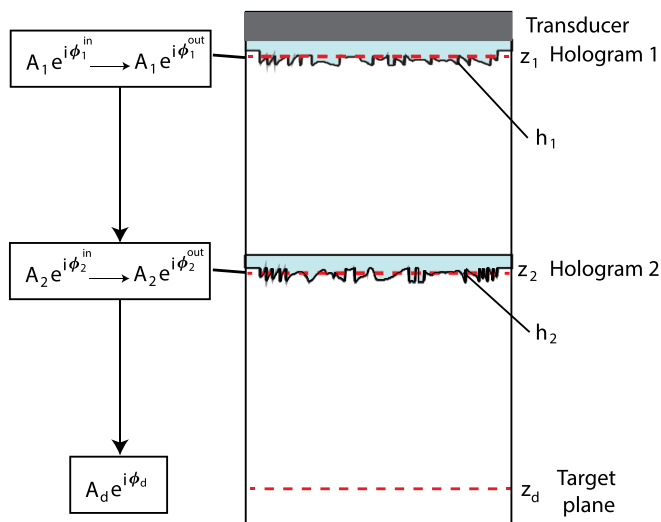


FIG. 1. (a) Geometry adopted for the two phase holograms. Annotations indicate the relative positions of the three planes  $z_1$ ,  $z_2$ , and  $z_d$  and other variables of the design process.

could in practice be three dimensional; however, for simplicity, only 2-D distributions were considered for this work.

For the first step, the target amplitude  $A_d(x, y)$ , phase  $\phi_d(x, y)$ , and depth  $z_d$  were defined along with a design frequency  $f$  and the positions of the first and second holograms  $z_1$  and  $z_2$ . The planar transducer was also assumed to lie in the  $z_1$  plane. Next, the target pattern  $A_d(x, y)e^{i\phi_d(x,y)}$  was back-propagated to the plane of the second hologram  $z_2$  using the angular spectrum method (ASM). The implementation used for this work was based on a spectral propagator with angular restriction as described by Zeng and McGough.<sup>17</sup> The relative positioning of each plane and hologram are shown in Fig. 1. The challenge then was to form the conjugate of the back-propagated field,  $A_2(x, y)e^{i\phi_2^{out}(x,y)}$ , over  $z_2$ .

To accomplish this, a phase map  $\phi_1^{out}(x, y)$  was sought for  $z_1$  which generated the modulus of the conjugate field  $A_2(x, y)$  over  $z_2$ . This was calculated using an iterative Fourier transform algorithm.<sup>10,18</sup> The algorithm was initialized by adding a random phase distribution  $\phi_2^{in}(x, y)$  to the target amplitude  $A_2(x, y)$  which was then projected to the plane  $z_1$ . The amplitude over  $z_1$  was replaced by the pressure incident from the transducer  $A_1(x, y)$ , while the phase  $\phi_1^{out}(x, y)$  was preserved. This altered field was then projected back to the plane  $z_2$ . Here, the amplitude was again replaced, in this case with the target amplitude  $A_2(x, y)$ , while the phase  $\phi_2^{in}$  was preserved. The process was then iterated to convergence.

As mentioned earlier, the coupling of waves into and out of the second hologram needs to be modeled when calculating  $\phi_1^{out}(x, y)$ . This was accomplished by using the k-Wave toolbox to evaluate the projection between the two planes.<sup>20</sup> This uses a k-space pseudospectral model for time domain simulations of acoustic waves. The simulation domain consisted of a half space of water and the hologram material. The plane  $z_2$  was located at depth  $b$ , representing the minimum thickness, below the water-hologram interface. Neither of the holograms physical profiles were modeled at this stage. (The ASM could alternatively have been modified to account for the water-hologram interface. The use of the k-Wave was to allow for exact registration with later simulations incorporating the hologram structures.)

Following the calculation of  $\phi_1^{out}$ , the first hologram profile  $h_1(x, y)$  was calculated to map the phase map  $\phi_1^{in}$  incident from the transducer onto the phase map  $\phi_1^{out}$  output by the optimization. This was done using

$$\text{mod}\{\phi_1^{out} - \phi_1^{in}\}_{2\pi} = (k_m - k_h)(h_m - h_1). \quad (1)$$

Here,  $k_h$  and  $k_m$  are the wavenumbers in the hologram and coupled medium (water), respectively, and  $h_m$  is the maximum hologram thickness. This approximates the hologram as a thin phase element.

The final step then was to calculate a profile  $h_2(x, y)$  for the second hologram to map the incident phase  $\phi_2^{in}$  over the plane  $z_2$  onto the target phase  $\phi_2^{out}$ . In principle,  $\phi_2^{in}$  was known from the output of the optimization. However, the thin phase approximation can become inaccurate as the size of structures on the hologram approaches the acoustic wavelength.<sup>18,19</sup> This could result in variations in the actual phase generated over the surface  $z_2$  by propagation through  $h_1$  compared to that predicted by the optimization. To correct for this, an additional simulation was conducted.

The profile  $h_1(x, y)$  was inserted into the simulation domain as a region with acoustic properties matching those of the hologram material. The transducer was represented by an appropriately shaped

source mask driven, with the uniform phase, at the design frequency  $f$ . This was placed in a water layer directly ( $100\ \mu\text{m}$ ) below the bottom of the first hologram which was coupled into the perfectly matched layer (PML), an absorbing layer surrounding the simulation grid which attenuates waves leaving the domain. The appropriate displacement for the profile  $h_1$  relative to the plane  $z_1$  used for the optimization was calculated from a separate simulation. The phase  $\phi_2^{\text{in}}$  over  $z_2$  was extracted from this simulation, and the second hologram profile was then calculated using Eq. (1).

To summarize, the design process consisted of the following steps:

1. Define the parameters  $A_d$ ,  $\phi_d$ ,  $z_d$ ,  $f$ ,  $z_1$ , and  $z_2$ .
2. Back-project  $A_d$ ,  $\phi_d$  to  $z_2$  to give target conjugate field  $A_2$ ,  $\phi_2^{\text{out}}$ .
3. Optimize  $\phi_1^{\text{out}}$  to generate  $A_2$  while allowing  $\phi_2^{\text{in}}$  to vary freely.
4. Calculate profile  $h_1$  to map  $\phi_1^{\text{in}} \rightarrow \phi_1^{\text{out}}$ .
5. Run full-wave simulation through  $h_1$  to give an updated estimate of  $\phi_2^{\text{in}}$ .
6. Calculate  $h_2$  to map  $\phi_2^{\text{in}} \rightarrow \phi_2^{\text{out}}$ .

The result of this process is two hologram profiles  $h_1$  and  $h_2$  which, from a known input source, combine to generate an arbitrary complex field at the surface of  $h_2$  when separated by the correct distance.

A test case was used to validate that this approach works experimentally. The target pattern, shown in Fig. 2, consisted of the letters UCL with the uniform amplitude and phase over the letters. This was designed for a circular 3.1 cm lead zirconate titanate (PZT) piston transducer (Olympus, Japan). The design frequency was 2.7 MHz. The target depth was 3 cm from second hologram surface  $z_2$ . The first hologram plane  $z_1$  was located a further 3 cm from  $z_2$ . The minimum thickness  $b$  was set to 0.3 cm (this defines the displacement of  $z_2$  from the back of the second hologram in the simulation). The sound speed and density of the hologram material were set to  $2495\ \text{ms}^{-1}$  and  $1190\ \text{kg m}^{-3}$ , respectively.<sup>21</sup> The values of  $1500\ \text{ms}^{-1}$  and  $1000\ \text{kg m}^{-3}$  were used for water.

Prior to design, the transducer output was characterized experimentally. This was done in a  $40 \times 40 \times 60\ \text{cm}^3$  test tank with a two axis computer controlled positioning system (Precision Acoustics, Dorchester, UK) using a calibrated 0.2 mm needle hydrophone (Precision Acoustics, Dorchester, UK). The transducer was driven



FIG. 2. Target pattern consisting of the letters UCL. Both the amplitude and phase are uniform across the letters.

using a signal generator (33522A, Agilent Technologies, Santa Clara, CA, USA) connected via a 75 W power amplifier (A075, E&I, Rochester, NY, USA). The driving signal was a 50 cycle sinusoid at the design frequency. The pressure was recorded over a  $40 \times 40\ \text{mm}^2$  plane parallel to the transducer with a step size of 0.25 mm. Time domain signals were recorded at each position using a digital oscilloscope with a sampling rate of 400 MHz and 32 averages. The steady state phase and amplitude values were extracted from the measurement data at each position. The field was then back-projected to the transducer surface with the ASM to use as the amplitude constraint  $A_1(x, y)$  for the plane  $z_1$ . The incident phase  $\phi_1^{\text{in}}$  was also known from this characterization. However, the angular variation over the surface was found to be extremely small, so to simplify the experimental design, avoiding the need to correct for rotation, it was approximated as uniform.

The calculated holograms were printed using a high-resolution PolyJet printer (Objet350 Connex, Stratasys, Eden Par) using veroClear as the hologram material. Prior to printing, an additional 1 mm backing was added to the design of the first hologram, and a 3 mm backing, representing the minimum thickness  $b$ , was added to the design of the second. A 1.4 cm square baffle was then added to both. To attach the first hologram to the transducer, the surrounding baffle was extruded down by a further 0.8 cm. To register and attach the two holograms together, four  $1 \times 1 \times 2.7\ \text{cm}^3$  columns were added to the first hologram at the corners of the baffle. A photograph of the assembled composite hologram attached to the front of the transducer can be seen in Fig. 3(a). Both hologram profiles are included in Fig. 2 in the supplementary material along with the predicted and target fields for the plane  $z_2$  from the optimization. The variation in the phase and amplitude formed at the target depth for different stages of the design process is shown in Fig. 3 in the supplementary material.

The acoustic field was then measured using the setup described above. The driving voltage was approximately 44 V peak-to-peak. A

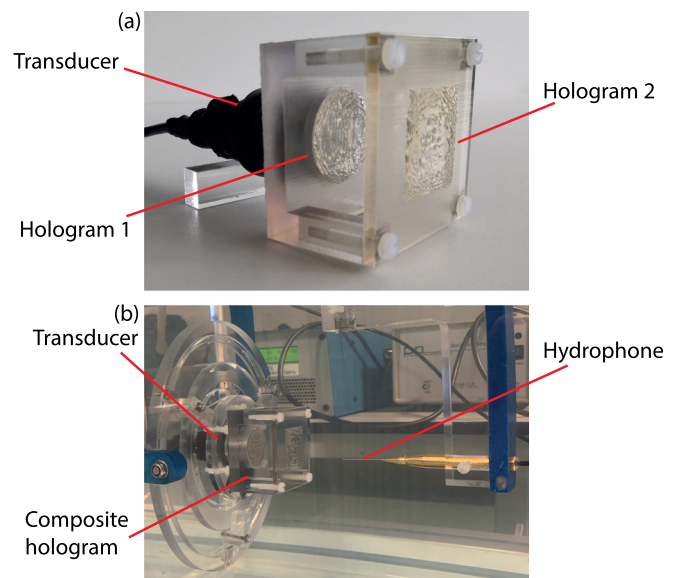


FIG. 3. (a) Photograph of a composite hologram attached to the front face of the PZT transducer. (b) Photograph of the experimental setup.

photograph of the experimental setup can be seen in Fig. 3(b). As before, the steady state phase and amplitude at the driving frequency were extracted from the measurements. The full 3-D wave-field was then calculated using the ASM. A simulation of the acoustic field generated by the composite hologram was also carried out using the k-Wave toolbox fully modeling propagation through both hologram profiles. A rigid transformation was then applied to align the simulated and experimental wave-fields.

The phase and amplitude generated experimentally over the target depth by the composite hologram can be seen in Figs. 4(a) and 4(b). The phase and amplitude generated in the simulation can be seen in Figs. 4(c) and 4(d). Both the target amplitude and phase distribution have been clearly generated in the experimental data, confirming that this approach works. However, neither distribution is completely uniform. In the experimental data, the amplitude varies by an average of 25%, while the phase varies by an average of  $14^\circ$ . For the simulated data, these values are 22% and  $8^\circ$ , respectively. The variation that would be expected from the perfect formation of the conjugate field, due to the diffraction limit, is 18% and  $5^\circ$ . The difference seen between the simulation and the theory suggests that, due to the limits of the thin element approximation, the conjugate field has been imperfectly formed.

The small difference between the simulated and experimental data could be the result of several factors. One possibility is errors in aligning or registering the position of the two holograms. To evaluate the possible impact of registration errors, a set of simulations were run systematically misplacing the position of the second hologram axially and laterally, in steps of  $100\ \mu\text{m}$ , relative to the first. For each simulation, the signal-to-noise (SNR), calculated as the ratio of the average pressure over the target pattern and the average background pressure, was evaluated. These simulations found that lateral errors have a

significant effect on the acoustic field. Errors of  $600\ \mu\text{m}$  caused the SNR to drop by  $>50\%$  with significant distortion occurring even for smaller misalignments. Much less sensitivity was found for axial errors. The SNR dropped by less than 30% for positional errors of 3 mm. Another possibility is the presence of shear waves in the experiment which were not modeled in the simulation. However, it is anticipated that this would not have a significant effect on the field. Waves are normally incident on the first hologram and incident principally at small angles for the second hologram. The clear formation of the target field in the experimental data supports this.

An additional numerical experiment was then used to assess the benefit of the approach introduced in this work compared to the use of a conventional holographic lens. The target pattern, depth, design frequency, and source properties for this experiment were identical to those used for the experimental test-case. The hologram was calculated directly from the phase of the back-propagated field  $\phi_2^{out}$  using Eq. (1). The acoustic field resulting from propagation through this hologram was then simulated using the k-Wave. The phase and amplitude generated over the target depth are shown in Figs. 5(a) and 5(b). It can be seen that the loss of amplitude modulation has resulted in the generation of side-lobes surrounding the target pattern along with large variations in amplitude over the pattern itself. Both the amplitude ( $38\%$ ) and phase ( $24^\circ$ ) vary to a greater degree than in the two hologram simulation.

After characterizing the acoustic field, the transmission losses for the composite hologram were approximated by using a radiation force balance (Precision Acoustics, United Kingdom) to measure the power transmitted by the transducer with and without the hologram attached. It was found that 83% of the energy was lost on transmission. This is due to interfacial losses on propagation through the 4 hologram surfaces along with acoustic attenuation in the hologram itself. In the future, these losses could be minimized by optimizing the choice of hologram material and refining the design. For example, the minimum thickness for both holograms could be reduced to decrease the effect of acoustic attenuation. The interfacial losses could be reduced with better matching between the hologram material and water. Alternatively, as shown in Fig. 1(c) in the [supplementary material](#), a reflection geometry could be employed for the two holograms using a material with a high acoustic impedance. The material for this work was chosen from those available on the high-resolution polyjet printer used for fabrication. Alternative fabrication methods such as computer-controlled machining,<sup>7</sup> casting,<sup>6</sup> and stereo-lithography<sup>22</sup>

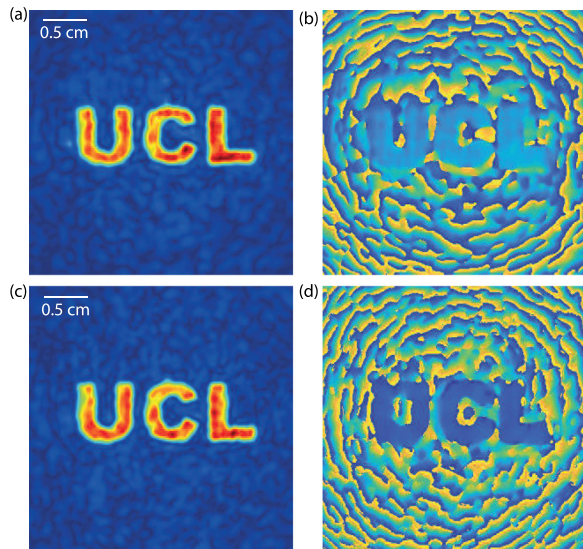


**FIG. 4.** (a) Amplitude of the field generated over the target depth by the composite hologram in the experiment. (b) Phase of the field generated over the target depth by the composite hologram in the experiment. (c) Amplitude of the field generated over the target depth by the composite hologram in simulation. (d) Phase of the field generated over the target depth by the composite hologram in simulation.

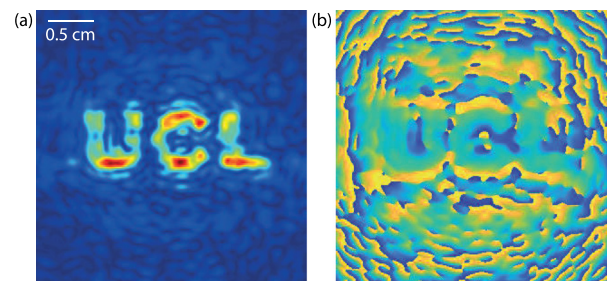


**FIG. 5.** (a) Amplitude of the field generated over the target depth by the single phase hologram. (b) Phase of the field generated over the target depth by the single phase hologram.

have already been reported for similar problems and could be explored in the future.

This work has demonstrated that the modulation of both the phase and amplitude of an incident acoustic wave can be achieved by using two separate phase holograms. This enables the efficient generation of arbitrary, complex, acoustic fields using a single acoustic source. The approach is narrowband (the variation in the SNR over the target plane with frequency is shown in Fig. 4 in the [supplementary material](#)), making it unsuited for applications requiring short tonebursts; however, it has the potential to impact a range of disciplines for which longer driving signals are utilized. For example, a number of works have recently reported the use of phase conjugate lenses for transcranial focusing.<sup>6,23</sup> However, it has been previously shown that compensating for the effect of absorption on the amplitude is important in order to fully correct for the distorting effect of the skull.<sup>24</sup> This could be achieved using the method reported here. Importantly for adoption, the geometry used to implement the technique here is simply adding only an extra displacement from the transducer surface compared to a conventional phase-conjugate lens. This enables it to be easily integrated within many existing experimental designs.

See the [supplementary material](#) for the illustrations of alternative experimental geometries along with further information on the profiles of the two fabricated holograms, the convergence of the optimization, and the performance of the composite hologram with frequency.

This work was supported by the Engineering and Physical Sciences Research Council. The author would like to thank Dr. Bradley Treeby and Dr. Ben Cox for helpful discussions.

## REFERENCES

- <sup>1</sup>T. Ilovitsh, A. Ilovitsh, J. Foiret, B. Fite, and F. Ferrara, *Nat. Commun. Biol.* **1**, 3 (2018).
- <sup>2</sup>J. Aubry, M. Tanter, M. Pernot, J. Thomas, and M. Fink, *J. Acoust. Soc. Am.* **113**, 84 (2003).
- <sup>3</sup>A. Marzo and B. Drinkwater, *Proc. Natl. Acad. Sci.* **116**, 84 (2019).
- <sup>4</sup>S. Inoue, S. Mogami, T. Ichiyama, A. Noda, Y. Makino, and H. Shinoda, *J. Acoust. Soc. Am.* **145**, 328 (2019).
- <sup>5</sup>S. Bobkova, L. Gavrilov, V. Khokhlova, A. Shaw, and J. Hand, *Ultrasound Med. Biol.* **36**, 888 (2011).
- <sup>6</sup>G. Maimbourg, A. Houdouin, T. Deffieux, M. Tanter, and J. Aubry, *Phys. Med. Biol. Lett.* **63**, 025026 (2018).
- <sup>7</sup>P. Kruizinga, P. van der Meulen, A. Fedjajevs, F. Mastik, G. Springeling, N. de Jong, J. Bosch, and G. Leus, *Sci. Adv.* **3**, e1701423 (2017).
- <sup>8</sup>K. Melde, A. G. Mark, T. Qiu, and P. Fischer, *Nature* **537**, 518 (2016).
- <sup>9</sup>R. Lalonde and J. Hunt, *IEEE Trans. Ultrason. Ferroelectr. Freq. Control* **40**, 592 (1993).
- <sup>10</sup>R. Leonardo, F. Ianni, and G. Ruocco, *Opt. Express* **15**, 1913 (2007).
- <sup>11</sup>M. Seldowitz, J. Allenbach, and D. Sweeney, *Appl. Opt.* **26**, 2788 (1987).
- <sup>12</sup>E. Bolduc, N. Bent, E. Santamato, E. Karimi, and R. Boyd, *Opt. Lett.* **38**, 3546 (2013).
- <sup>13</sup>D. Bowman, T. Harte, V. Chardonnet, C. De Groot, S. Denny, G. Le Goc, M. Anderson, P. Ireland, D. Cassettari, and G. Bruce, *Opt. Express* **25**, 11692 (2017).
- <sup>14</sup>M. Fink, D. Cassereau, A. Derode, C. Prade, P. Roux, M. Tanter, J. Thomas, and F. Wu, *Rep. Prog. Phys.* **63**, 1933 (1999).
- <sup>15</sup>H. Bartelt, *Appl. Opt.* **23**, 1499 (1984).
- <sup>16</sup>A. Jesacher, C. Maurer, A. Schwaighofer, S. Bernet, and M. Ritsch-Marte, *Opt. Express* **16**, 2597 (2008).
- <sup>17</sup>X. Zeng and R. McGough, *J. Acoust. Soc. Am.* **123**, 68 (2008).
- <sup>18</sup>S. D. Mellin and G. P. Nordin, *Opt. Express* **8**, 705 (2001).
- <sup>19</sup>M. D. Brown, B. T. Cox, and B. E. Treeby, *Appl. Phys. Lett.* **111**, 244101 (2017).
- <sup>20</sup>B. E. Treeby and B. T. Cox, *J. Biomed. Opt.* **15**, 021314 (2010).
- <sup>21</sup>M. Brown, D. Nikitichev, B. Treeby, and B. Cox, *Appl. Phys. Lett.* **110**, 094102 (2017).
- <sup>22</sup>J. Janjic, P. Kruizinga, P. Meulen, G. Springeling, F. Mastik, G. Leus, J. Bosch, A. van der Steen, and G. Soest, *Appl. Phys. Lett.* **112**, 251901 (2018).
- <sup>23</sup>M. Ferri, J. Bravo, J. Redondo, and J. Sanchez-Perez, *Ultrasound Med. Biol.* **45**, 867 (2019).
- <sup>24</sup>M. Tanter, J. Thomas, and M. Fink, in *IEEE Ultrasonics Symposium Proceedings* (1996), p. 5658305.